Noise Processes and Nonlinear Mechanisms in Optoelectronic Phase-Locked Loop Using a Balanced Optical Microwave Phase Detector

Meysam Bahmanian and J. Christoph Scheytt, *Member, IEEE*

***Abstract*— This article analyses the effect of noise and nonlinearity in optoelectronic phase-locked loops (OEPLLs). The OEPLL phase-locks a microwave oscillator on the envelope of the optical pulse train from a mode-locked laser (MLL). The phase detector of this type of OEPLL is called a balanced optical microwave phase detector (BOMPD) and operates in a mixed electro-optical domain. The main noise sources in a BOMPD, such as shot noise of photodiodes, generation-recombination noise of photodiodes, relative intensity noise of the laser, and noise of the bias voltage applied to the BOMPD. are discussed. The nonlinear behavior of the BOMPD with respect to the intensity of the optical field and the amplitude of the RF voltage is discussed. An OEPLL that can lock on the harmonics and interharmonics of the MLL repetition rate is demonstrated. The OEPLL has an in-band phase noise of below −150 dBc/Hz at 100-kHz offset frequency for a carrier frequency of 10 GHz. This phase noise level is 10–20 dB better than state-of-the-art commercial frequency synthesizers.**

***Index Terms*— Frequency synthesizer, generation-recombination (GR) noise, harmonic locking, interharmonic locking, low phase noise, mode-locked laser (MLL), nonlinearity, optoelectronic phase-locked loop (OEPLL), phase-locked loop, photodiode, shot noise.**

I. Introduction

OPTICAL pulses from mode-locked lasers (MLLs) have attracted attention for a wide range of applications because of their special properties, such as extremely short pulsewidth, high peak power, and excellent jitter. Extremely wideband pulses of MLLs have made optical frequency metrology down to Hertz resolution possible and connected the frequency measurement link between the microwave domain and the optical domain [1], [2], [3]. In addition, MLLs have found their way to a wide range of applications such as frequency comb spectroscopy, optical sampling, photonic analog-to-digital converters (ADCs), photonic radar, and ultralow-noise microwave signal generation [4], [5], [6], [7], [8], [9], [10], [11], [12], [13], [14], [15], [16], [17].

The wide frequency spectrum of an MLL signal can potentially be used for low noise and wideband microwave frequency synthesis. A simple approach for MLL-based microwave signal generation is the direct detection scheme using a single photodiode. This method is capable of synthesizing any harmonic of the repetition rate of the MLL; however, high-energy pulses of the MLL significantly reduce the bandwidth of the photodiode due to the space-charge nonlinear effect [18], [19], [20], [21]. Filtering the subharmonics of the synthesized signal can also be a tedious task for wideband frequency synthesis. Reducing the pulse energy by increasing the repetition rate using the pulse interleaving technique mitigates the nonlinear effects in the photodiode and increases the bandwidth while keeping the average intensity of the optical pulse unchanged [15], [16]. Although higher repetition rates make filtering the subharmonics easier, fewer frequencies are available to be selected. Filtering the subharmonics can be especially difficult for wideband frequency synthesis, which requires a tunable narrowband filter.

Another approach for wideband MLL-based microwave signal generation is to phase-lock a microwave tunable oscillator to the envelope of the pulse train of an MLL by means of an optoelectronic phase-locked loop (OEPLL) [22], [23], [24]. The bandwidth of such a loop is usually below 10 MHz, which can easily filter the frequency components of the intensity waveform of the MLL with repetition rates in the range of hundreds of megahertz. The OEPLL requires a phase detector in a mixed electro-optical domain, a so-called balanced optical microwave phase detector (BOMPD). A low-noise OEPLL using such a phase detector has been reported using a fiber-Sagnac-modulator-based BOMPD and a dielectric resonator oscillator (DRO) locked to a harmonic of the repetition rate of the MLL [17], [24], [25]. Further implementation of OEPLLs with higher phase noise has been reported for single frequency synthesis [22], [23], [26]. The first wideband OEPLL has been reported in [27] using a semiconductor voltage-controlled oscillator (VCO) capable of locking on any harmonic of the repetition rate of the MLL in the frequency range of 5–10 GHz. Further improvement of phase noise and frequency range of this scheme has been reported in [28] covering more than three octaves of the band from 2–20 GHz. Enhancement of the frequency resolution by locking on interharmonics (noninteger harmonics) of the

Manuscript received 4 February 2022; revised 27 May 2022; accepted 3 July 2022. Date of publication 19 August 2022; date of current version 5 October 2022. This work was supported in part by Deutsche Forschungsgemeinschaft (DFG) within the projects "Optoelectronic Frequency Synthesizer with Femtosecond Diode Laser" (OFFeDi) under Grant 370491995 and "Active THz Transceiver Components" under Grant 403579441 within the Research Unit FOR 2863 "Metrology for THz Communications" (METERACOM) and "MLL-Basierte Integrierte THz Frequenz-Synthesizers" (MINTS) under Grant 469044319. *(Corresponding author: Meysam Bahmanian.)*

The authors are with the System and Circuit Technology Group, Heinz Nixdorf Institute, Paderborn University, 33102 Paderborn, Germany (e-mail: meysam.bahmanian@uni-paderborn.de).

Color versions of one or more figures in this article are available at https://doi.org/10.1109/TMTT.2022.3197621.

Digital Object Identifier 10.1109/TMTT.2022.3197621

This work is licensed under a Creative Commons Attribution 4.0 License. For more information, see https://creativecommons.org/licenses/by/4.0/

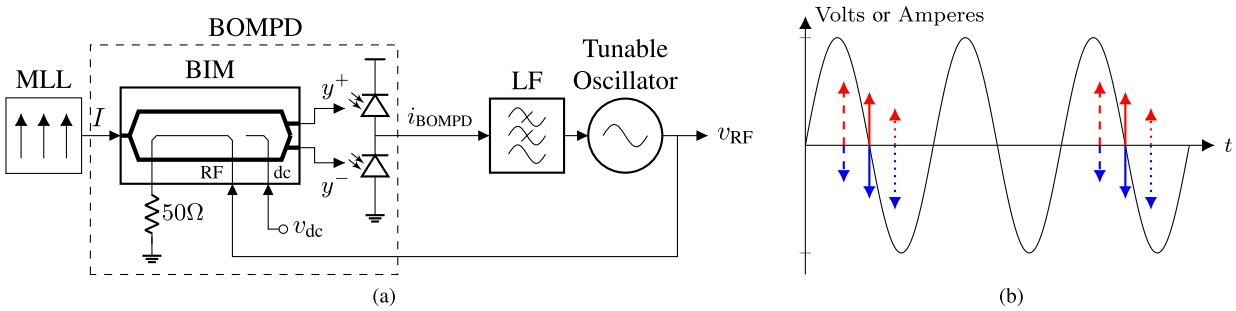

Fig. 1. (a) Simplified block diagram of the OEPLL and (b) corresponding waveforms: black: voltage waveform at the RF port of BIM; red: upper photodiode current; blue: lower photodiode current when (solid) the phase of RF signal and the optical intensity are aligned; dashed: the optical intensity has a phase lead; and dotted: the optical intensity has a phase lag. MLL: mode-locked laser. BIM: balanced intensity modulator. LF: loop filter. BONPD: balanced optical microwave phase detector.

MLL repetition rate has also been reported in [29]. This type of OEPLL employs a different operating regime of the BOMPD, which internally generates harmonics of the RF signal, necessary for interharmonic locking.

The low-jitter MLLs and OEPLLs with low phase noise have shown their potential for low-phase-noise microwave generation, and the BOMPD stands at the core of OEPLL. Hence, a good understanding of its dynamics is the key to the implementation of low-phase-noise OEPLLs as the phase noise of the BOMPD directly affects the inside-loop phase noise of the output microwave signal. In [30], the dynamics of the loop have been explained, and the characteristic function of the BOMPD has been derived. However, phase noise in the BOMPD and the nonlinear mechanisms that affect its performance still need to be addressed. In this article, we focus on different noise processes and nonlinear mechanisms that affect the performance of the BOMPD. In Section II, we explain the operating principle of the OEPLL and define the variables and fundamental relations necessary for noise and nonlinearity discussions. Section III addresses different noise sources in the BOMPD, such as shot noise and generation-recombination (GR) noise of the photodiodes, relative intensity noise (RIN) of MLL, and noise of the dc voltage applied to the modulator. The effects of these noise sources on the overall phase noise of the BOMPD are shown, and the results are discussed. In Section IV, nonlinear effects with respect to optical and RF inputs of the BOMPD are discussed. Finally, in Section V, an implementation of the OEPLL is demonstrated, which can lock on the harmonics and interharmonics of the optical reference repetition rate. The OEPLL in-band phase noise is below −150 dBc/Hz at 100-kHz offset frequency for a carrier frequency of 10 GHz. This phase noise level is 10–20 dB below that of the state-of-the-art commercial frequency synthesizers.

II. Theory of Operation

Fig. 1(a) shows the simplified block diagram of the OEPLL. The BOMPD operates in a mixed electro-optical domain and samples the RF signal of a tunable oscillator using a balanced intensity modulator (BIM), which can be a fiber-Sagnac loop or a Mach–Zehnder modulator (MZM). These intensities are converted to a current via a pair of photodiodes and carry the information about the phase difference between the RF signal and the MLL intensity waveform. These current pulses are then integrated via a loop filter to extract the dc term and fed back to the tunable oscillator to align its phase with the optical reference and close the loop. Fig. 1(b) shows the RF signal and the optical pulses of the upper and lower photodiodes. If the phase of the tunable oscillator is not aligned with the optical reference, the photodiode currents will not be equal. This leads to the generation of a dc current, which is integrated at the loop filter, and generates an error voltage, which realigns the tunable oscillator phase with the optical reference. Further details on the loop dynamics can be found in [30].

The output intensities of a lossless balanced MZM, I_y^+ and I_y^-, can be written as

$$I_y^{\pm} = \frac{I(t)}{2}\left[1 \pm \sin(\psi)\right] \tag{1}$$

where $I(t)$ is the intensity (optical cycle averaged) of the optical input and ψ is the total optical phase shift between the modulator arms, which is proportional to the dc and the RF modulation voltages

$$\psi = \psi_{RF} + \psi_{dc} = \frac{v_{RF}\pi}{V_{\pi,RF}} + \frac{v_{dc}\pi}{V_{\pi,dc}} \tag{2}$$

where ψ_{dc} is the optical phase shift introduced by the dc electrode, ψ_{RF} is the optical phase shift introduced by the RF electrode, $V_{\pi,dc}$ is the π-voltage of the dc electrode, $V_{\pi,RF}$ is the π-voltage of RF electrode, v_{dc} is the bias voltage at the dc electrode, and v_{RF} is the RF modulation voltage waveform. The MLL intensity waveform can be written as

$$I(t) = I_0 T_{ref} \sum_{m=-\infty}^{+\infty} P\left(t - \frac{m}{f_{ref}}\right) \tag{3}$$

where I_0 is the average intensity of the optical input, $f_{ref} = 1/T_{ref}$ is the repetition rate of the optical pulses, and $P(t)$ is the energy normalized pulse shape such that

$$\int_{-T_{ref}/2}^{+T_{ref}/2} dt\, P(t) = 1. \tag{4}$$

We assume single tone modulation of the RF electrode with an angular frequency of ω_{RF}, an amplitude of V_{RF}, and an offset phase of ϕ

$$v_{RF} = V_{RF}\sin(\omega_{RF}t + \phi). \tag{5}$$

The characteristic function of the BOMPD is defined as its average output current as a function of the phase difference

between the RF signal and the MLL desired harmonic

$$H(\phi) = \left\langle i_{\mathrm{PD}}^{+} - i_{\mathrm{PD}}^{-} \right\rangle \tag{6}$$

where $\langle . \rangle$ denotes temporal averaging, and i_{PD}^{+} and i_{PD}^{-} are the upper and lower photodiode currents, respectively. The phase detector can discriminate the phase difference between the N'th harmonic of the reference and the RF signal, which requires $\omega_{\mathrm{RF}} = N\omega_{\mathrm{ref}}$, where $\omega_{\mathrm{ref}} = 2\pi f_{\mathrm{ref}}$. With these assumptions, the characteristic function of the BOMPD can be written as [30]

$$H(\phi) = I_0 R_\lambda \sin\left[\alpha \sin(\phi) + \psi_{\mathrm{dc}}\right] \tag{7}$$

where R_λ is the responsivity of the photodiode and

$$\alpha = v_{\mathrm{RF}} \pi / V_{\pi,\mathrm{RF}}. \tag{8}$$

When the OEPLL is locked, the output current of the BOMPD becomes zero for a type II loop filter configuration [31]. This requires $\psi_0 = 0$, where we defined ψ_0 as

$$\psi_0 = \psi_{\mathrm{dc}} + \alpha \sin(\phi). \tag{9}$$

Hence, the BOMPD gain K_ϕ is especially important at the zero crossing of the characteristic function [30]

$$K_\phi = I_0 R_\lambda \sqrt{\alpha^2 - \psi_{\mathrm{dc}}^2}\,. \tag{10}$$

Therefore, the BOMPD gain is proportional to the average intensity of the optical field and is maximized when $\psi_{\mathrm{dc}} = 0$.

III. Noise in BOMPD

There are three main sources of noise that affects the performance of the BOMPD: the noise of the photodiodes, RIN of the laser, and the noise of dc voltage applied to the dc electrode of MZM. These noise sources have different behaviors and transfer characteristics that are addressed in this section.

In order to formulate the effect of these noise sources on the BOMPD performance, we first quantify the power spectral density (PSD) of the noise current at the output of the BOMPD. Taking into account this noise current, the output current of the BOMPD can then be written as

$$i_{\mathrm{out}}(t) = H(\phi) + i_n(t) \tag{11}$$

where $i_{\mathrm{out}}(t)$ is the output current of the BOMPD, $H(\phi)$ is the characteristic function of the BOMPD given in (7), and $i_n(t)$ is the output noise current. In the proximity of the operating point of the BOMPD, $H(\phi)$ can be approximated as

$$H(\phi) \approx K_\phi \times \phi. \tag{12}$$

Substituting this approximation into (11) gives

$$i_{\mathrm{out}}(t) = K_\phi \left(\phi + \frac{i_n(t)}{K_\phi}\right). \tag{13}$$

The first term in parentheses on the right-hand side of (13) is the phase difference between the desired harmonic of the envelope of the optical pulse train and the RF signal. The second term is the output noise current of the BOMPD translated into the phase domain and is called the phase noise of the BOMPD. Like many other random processes, it is practical to talk about the PSD of phase noise, rather than its instantaneous value. The PSD of the phase noise of the BOMPD can be written as

$$S_{\phi_n}(f) = \frac{S_{i_n}(f)}{K_\phi^2} = \frac{S_{i_n}(f)}{I_0^2 R_\lambda^2 \left(\alpha^2 - \psi_{\mathrm{dc}}^2\right)} \tag{14}$$

where $S_{i_n}(f)$ is the PSD of the output noise current $i_n(t)$ and $S_{\phi_n}(f)$ is the PSD of the *equivalent* phase noise caused by this current noise. We also substituted K_ϕ from (10) to (14). With this approach, all we have to do is to find the output noise current caused by different mechanisms in the BOMPD. The phase noise caused by these mechanisms is then found using the relation in (14).

A. Shot Noise of Photodiodes

Shot noise of photodiodes is considered to be the main source of noise in the BOMPD, which cannot be avoided—adapting a classical point of view and assuming that the light is in a coherent state [32]. Although shot noise is well studied and modeled as a Poisson process, treatment of nonstationary noise due to pulsed mode stimulation of the photodiodes used in the BOMPD requires further attention. This Poisson process can be estimated as a Gaussian process since, in BOMPD, we are dealing with a very high number of photons. In order to model the nonstationary shot noise, first, the time-dependent output intensities of the BOMPD are determined. From these intensities, the *instantaneous* variance of the nonstationary shot noise of the photodiode currents is calculated. This instantaneous variance is then decomposed into two terms: a deterministic time variant window function multiplied by a stationary Gaussian noise. This decomposition is the key to deriving the autocorrelation function and the PSD of the nonstationary photodiode noise current.

The pulse widths of MLLs are typically below 1 ps, which is at least 25 times shorter than the RF signal period in the microwave band up to the 40-GHz frequency range. Therefore, the modulation term in (1), $1 \pm \sin(\psi)$, is considered approximately constant during the time interval when it is sampled by the MLL pulses. The harmonic locking condition, $\omega_{\mathrm{RF}} = M\omega_{\mathrm{ref}}$ for a positive integer M, leads to a sampling of the modulation term at the same phase. Therefore, the modulation term in (1) can be considered as constant. Substituting (3) into (1) under this assumption, the output intensities of the modulator can be written as

$$I_y^{\pm} = \frac{1}{2} I_0 T_{\mathrm{ref}} \left[1 \pm \sin(\psi_0)\right] \sum_{m=-\infty}^{+\infty} P\left(t - \frac{m}{f_{\mathrm{ref}}}\right) \tag{15}$$

where $I_y^{\pm}$ denotes the intensity of the modulator outputs $y^{\pm}$ in Fig. 1(a) and ψ_0 is given in (9). The photodiode converts the photons into electron–hole pairs. Generation of charge carriers with photons has Poisson statistics and generates shot noise [32, Ch. 3]. These charge carriers travel toward the photodiode junctions with different velocities. This leads to the widening of the optical pulse at the photodiode, the so-called transit-time spread [33, Ch. 17]. These mechanisms are included in the linear model of the photodiode illustrated in Fig. 2(a). The photodiode shot noise $i_{n,y}$ is added after

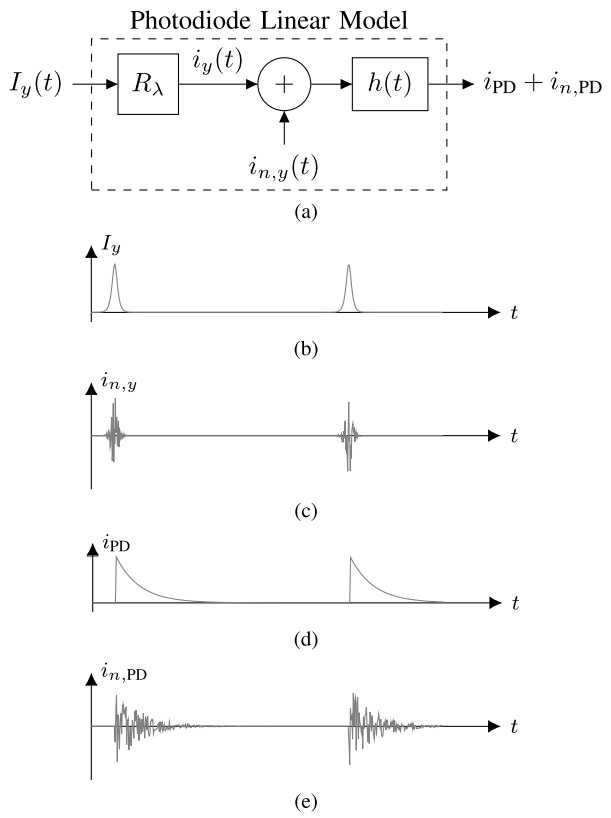

Fig. 2. (a) Linear model of photodiode including shot noise. (b) Intensity of the incident beam generated by a femtosecond laser. (c) Generated shot noise before getting shaped by photodiode response. (d) Output current pulses of the photodiode. (e) Shot noise of the photodiode.

linear generation of charge carriers modeled by a constant responsivity R_λ. The transit-time spread is modeled by a lossless linear time-invariant block with an impulse response of $h(t)$ that does not recombine or generate charge carriers, and therefore,

$$\int_0^\infty dt h(t) = 1. \tag{16}$$

Using this linear model, the output current of the upper and lower photodiodes can be written as

$$i_{\mathrm{PD}}^{\pm} = \frac{1}{2} I_0 T_{\mathrm{ref}} R_\lambda \left[1 \pm \sin(\psi_0)\right] \sum_{m=-\infty}^{+\infty} P\left(t - \frac{m}{f_{\mathrm{ref}}}\right) * h(t) \tag{17}$$

where $*$ denotes the convolution operation.

The optical pulses of MLL have a much lower effective temporal width than the photodiode impulse response. Therefore, the optical pulse shape $P(t)$ can be approximated as the Dirac delta function, and the photodiode currents become

$$i_{\mathrm{PD}}^{\pm} = \frac{1}{2} R_\lambda I_0 T_{\mathrm{ref}} \left[1 \pm \sin(\psi_0)\right] \sum_{m=-\infty}^{+\infty} h\left(t - \frac{m}{f_{\mathrm{ref}}}\right). \tag{18}$$

When the OEPLL is locked, the output intensities of the BOMPD become equal or equivalently $\psi_0 = 0$. The output currents of the upper and lower photodiodes, $i_{\mathrm{PD}}^{\pm}$, consequently become equal

$$i_{\mathrm{PD}}^{\pm} = \frac{1}{2} R_\lambda I_0 T_{\mathrm{ref}} \sum_{m=-\infty}^{+\infty} h\left(t - \frac{m}{f_{\mathrm{ref}}}\right). \tag{19}$$

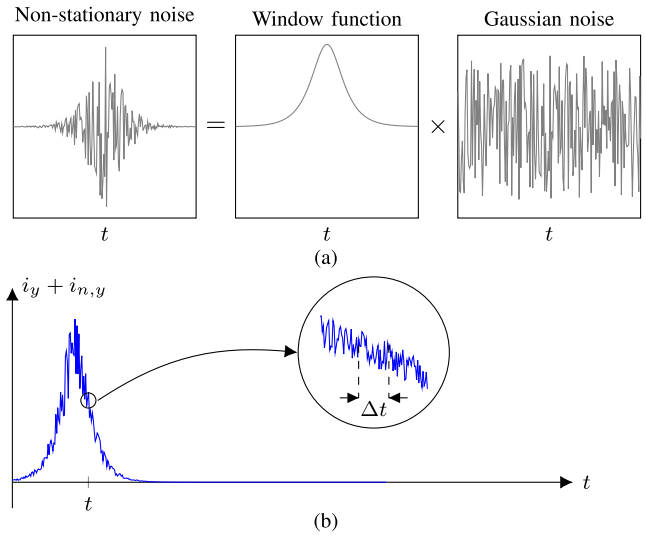

Fig. 3. (a) Decomposition of nonstationary shot noise into the product of a deterministic window function and Gaussian noise. (b) Quasi-stationary approximation of the optical pulse in a short interval of Δt.

Now, the photodiode currents are derived, and we are ready to find the shot noise. The shot noise of the optical pulse is not stationary, and its properties vary with respect to time. Therefore, we employ a quasi-stationary approach to find the PSD of the current noise. The probability of detection of a photon at a certain time is statistically independent of the detection of a photon at any time earlier. Therefore, the shot noise $i_{n,y}(t)$ can be factorized as a product of a white Gaussian process, which is memoryless and models the statistical independency of detection of the photons, and a time-varying deterministic window function, which models the nonstationary behavior of $i_{n,y}(t)$. This decomposition of nonstationary noise is illustrated graphically in Fig. 3(a). If we consider a short time slot Δt in the neighborhood of t, the intensity of the pulse can be considered as constant. This assumption is also illustrated graphically in Fig. 3(b). The instantaneous variance of the noise can then be written as

$$\begin{aligned} \mathrm{E}\left[i_{n,y}^2(t)\right] &= 2q i_y(t) \Delta f \\ &= q R_\lambda I_0 T_{\mathrm{ref}} \sum_{m=-\infty}^{+\infty} P\left(t - \frac{m}{f_{\mathrm{ref}}}\right) \Delta f \end{aligned} \tag{20}$$

where E[.] denotes the expectation value, q is the electron charge, and Δf is the noise bandwidth (note that time and frequency are orthogonal, and reducing temporal resolution corresponds to increasing spectral range; in other words $\Delta f \gg (\Delta t)^{-1}$ has to be satisfied for the quasi-stationary approximation in (20) to be valid). We also suppressed the upper $\pm$ index as the currents of the lower and upper photodiodes are equal and have the same stochastic properties. We decompose the noise current $i_{n,y}$ into two terms, i_n and $w(t)$, such that

$$i_{n,y}(t) = i_n(t) w(t) \tag{21}$$

where $w(t)$ is a deterministic window function, which models the nonstationary behavior of the noise current, and i_n is a white Gaussian noise current with a **single-sided** PSD of qRI_0. The autocorrelation function of this noise current according to the Wiener–Khinchin theorem is the inverse Fourier transform of its PSD

$$R_{i_n}(t,t') = \mathrm{E}\big[i_n(t)i_n(t')\big] = \frac{1}{2}qR_\lambda I_0\delta(t-t'). \tag{22}$$

Now, we find the window function $w(t)$ such that the variance of the noise current in (21) is equal to the noise current variance in (20). The variance of (21) can be written as

$$\mathrm{E}\big[i_{n,y}^2(t)\big] = w^2(t)\mathrm{E}\big[i_n^2(t)\big] = w^2(t)qR_\lambda I_0\Delta f. \tag{23}$$

By comparing (20) and (23), the time varying window function $w(t)$ can be determined

$$w(t) = \sqrt{T_{\mathrm{ref}}\sum_{m=-\infty}^{+\infty} P\left(t-\frac{m}{f_{\mathrm{ref}}}\right)}. \tag{24}$$

If we assume the optical pulses do not overlap, (24) can be further simplified

$$w(t) = \sum_{m=-\infty}^{+\infty}\sqrt{T_{\mathrm{ref}}P\left(t-\frac{m}{f_{\mathrm{ref}}}\right)}. \tag{25}$$

Equations (24) and (25) show that the photodiode noise current is proportional to the square root of the pulse shape, $P(t)$. Now, using (21), the autocorrelation function of the nonstationary noise current $i_{n,y}$ can be found

$$\begin{aligned} R_{i_{n,y}}(t,t') &= \mathrm{E}\big[i_{n,y}(t)i_{n,y}(t')\big] \\ &= \frac{1}{2}qR_\lambda I_0\delta(t-t')w(t)w(t'). \end{aligned} \tag{26}$$

The dependence of $R_{i_{n,y}}(t,t')$ to t and t' rather than their difference $t-t'$ is because of nonstationary nature of the pulsed noise current $i_{n,y}$. The single-sided PSD of the noise current is

$$\begin{aligned} S_{i_{n,y}}(f) &= \mathrm{E}\left[\lim_{T\to\infty}\frac{1}{T}\left|\int_{-T}^{+T} dt\, i_{n,y}(t)e^{j\omega t}\right|^2\right] \\ &= \lim_{T\to\infty}\frac{1}{T}\int_{-T}^{+T}\int_{-T}^{+T} dt\,dt'\,\mathrm{E}[i_{n,y}(t)i_{n,y}(t')]e^{j\omega(t-t')} \end{aligned} \tag{27}$$

where $\omega = 2\pi f$. Substituting (26) into (27) and using the relation between the window function and the pulse shape in (25) and the normalizing condition in (4), the single-sided PSD of the noise current can be found

$$\begin{aligned} S_{i_{n,y}}(f) &= \frac{1}{2}qR_\lambda I_0\lim_{T\to\infty}\frac{1}{T}\int_{-T}^{+T} dt\,w^2(t) \\ &= qR_\lambda I_0. \end{aligned} \tag{28}$$

Therefore, the shot noise $i_{n,y}$ has a well-defined PSD although it is not a stationary process. The magnitude of this PSD is equal to the PSD generated by a continuous wave optical field with an intensity of $I_0/2$. The intensity of this CW optical field is equal to the average intensity of the pulsed optical field $I_y(t)$. Therefore, only the average intensity affects the shot noise PSD. The reason that shot noise is independent of the pulse shape is that its instantaneous variance is proportional to the photocurrent current. This consequently leads to the proportionality of the window function to the *square root* of the pulse shape. The pulse shape is once again squared in the derivation of its PSD, in (26)–(28), and then integrated. This sequence of mathematical operations that naturally occurs in the photodiode demonstrates the shot noise independence of the optical pulse shape.

The noise current $i_{n,y}$ generated in the illumination region of the photodiode is then shaped by the linear time-invariant block in Fig. 2(a), which models the transit-time spread with an impulse response of $h(t)$. Therefore, the single-sided PSD of the output noise current is

$$S_{i_{n,\mathrm{PD}}}(f) = S_{i_{n,y}}(f)|H(f)|^2 = qR_\lambda I_0|H(f)|^2 \tag{29}$$

where $H(f)$ is the Fourier transform of $h(t)$. The result in (29) is identical to what has been derived by Quinlan *et al.* [34], where the detection process is treated semiclassically. In [34], the incident beam is made of photons that are detected at the photodiode with a certain probability in a short time interval. The detection probability, consequently, leads to randomization of detection and, hence, shot noise. In contrast, we employed a fully classical approach where the incident beam is an optical field (*not photons*) with a certain intensity that is detected at the photodiode. By assuming the shot noise of a CW optical field in (20) for our quasi-stationary approach, we avoided the discretization of light. Also, the stationary assumption in (20) in a short interval of Δt is equivalent to the assumption of single photon detection in a sufficiently short interval in the semiclassical approach in [34]. One advantage of our fully classical approach is that it can be generalized to nonstationary processes that have a defined PSD in a short time interval. As we will see in Section III-B, this approach is especially helpful to treat nonstationary GR noise.

For phase detector application, the shot noise of the photodiode is important inside the loop bandwidth, which is usually below 10 MHz. The bandwidth of the photodiode is usually much higher than the loop bandwidth; therefore, $H(f)$ in (29) can be approximated as 1. The single-sided PSD of the output noise current of the BOMPD is the superposition of the upper and lower photodiode shot noise currents that are statistically independent

$$S_{i_{n,\mathrm{shot}}}(f) = 2qR_\lambda I_0. \tag{30}$$

The phase noise of the BOMPD can then be found using the relation in (14) as

$$S_{\phi_{n,\mathrm{shot}}}(f) = \frac{S_{i_{n,\mathrm{shot}}}(f)}{K_\phi^2} = \frac{2q}{R_\lambda I_0\left(\alpha^2-\psi_{\mathrm{dc}}^2\right)} \tag{31}$$

where $S_{\phi_n}(f)$ is the phase noise of the BOMPD. The photodiode dark current has a negligible effect on the phase noise because the main contributor to the photodiode currents is the incident beam from the MLL. Taking into account the dark current, (30) can be rewritten as

$$S_{i_{n,\mathrm{shot}}}(f) = 2q(R_\lambda I_0 + 2I_{\mathrm{dark}}) \tag{32}$$

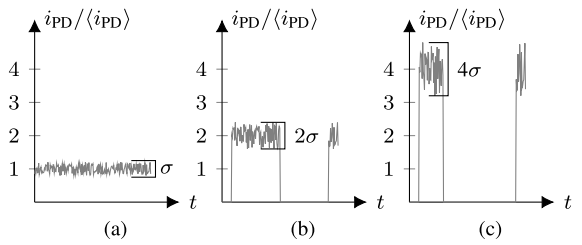

Fig. 4. Qualitative illustration of the effect of duty cycle on GR noise of photodiode: (a) continuous-wave, (b) 50% duty cycle, and (c) 25% duty cycle photocurrents.

where I_{dark} is the dark current of a single photodiode. The dark current is in the range of nanoamperes, while the beam-induced photocurrent is in the range of at least hundreds of microamperes. Thus, it is a fair approximation to neglect the photodiodes' dark current.

Shot noise of photodiodes puts a theoretical limit on the phase noise of the BOMPD (assuming that the light is in a coherent state). However, there are undesired effects that can lead to phase noise degradation in the BOMPD above the shot noise limit. In the following, we discuss other sources of noise in the BOMPD and their transfer characteristics.

B. Generation-Recombination Noise

In addition to shot noise, photodiodes have a random variation of charge carriers due to the GR of charge carriers. While the PSD of shot noise is proportional to the photocurrent, the GR-noise PSD is proportional to the square of the photocurrent and may exceed shot noise at high optical excitation levels. The two-sided PSD of GR noise of an intrinsic semiconductor stimulated with a CW optical field, $S_{i,\text{GR-CW}}$, can be written as [35], [36]

$$S_{i_{\text{GR-CW}}}(f) = \frac{2i_{\text{PD}}^2\tau}{n_0(1+\omega^2\tau^2)} \tag{33}$$

where $\omega = 2\pi f$, i_{PD} is the photocurrent, n_0 is the number of free carriers in equilibrium, and τ is the decay time.

When the active region of the photodiode is illuminated with an optical pulse, electron–hole pairs are generated. On the one hand, the built-in electric field and the external field (caused by the external dc supply) of the photodiode separate these charge carriers and move them toward the photodiode's external junctions. This mechanism is linear, and the difference between the mobility of electrons and holes contributes to the overall photodiode transit time and limits its bandwidth. On the other hand, the Coulomb interaction between electrons and holes creates a counteracting electric field that attracts electrons and holes to each other. This attraction force is a function of the optical beam intensity, which makes it a nonlinear mechanism and leads to the dependence of the transit time on the optical intensity. Generation and recombination of charge carriers occur at this level, where the charge carriers are still in the active region. The nonlinearity of photodiode under high excitation levels, consequently, makes the dynamics of GR noise both nonlinear and a function of time. This level of complexity is an obstacle to providing a general formula for GR noise under pulsed excitation although a formula for the PSD of GR noise under CW excitation of photodiodes is available. Our aim here is to illustrate qualitatively, with some simplified assumptions, how pulsed excitation causes enhancement of GR noise. The GR-noise enhancement consequently limits the phase noise improvement in BOMPD when the average intensity is increased, which is expected if only shot noise is taken into account.

The quadratic dependence of GR noise PSD to the photocurrent has another undesired effect on the photodiode noise when the excitation beam is an optical pulse. This effect is illustrated graphically in Fig. 4, where the photodiode GR noise is shown for photocurrent waveforms with the same average but with different duty cycles (γ). On time scales longer than τ, the variance of GR noise is proportional to the instantaneous photocurrent, which scales with $1/\gamma$. The PSD of GR noise, on the one hand, is proportional to the noise variance (during the presence of the optical pulse), which scales with $1/\gamma^2$ and, on the other hand, is proportional to γ because of temporal averaging. Therefore, the PSD of GR noise is inversely proportional to the pulse duty cycle γ. It is noteworthy that, under the same conditions, during the presence of photocurrent, the instantaneous variance of the shot noise scales with $1/\gamma$, which makes the shot noise PSD independent of pulse shape and duty cycle, as discussed in Section III-A.

The behavior of GR noise with respect to the duty cycle of the photocurrent can also be shown mathematically with some simplified assumptions. We assume that the photocurrent pulse train has a rectangular shape and a duty cycle of γ, and has an average of $\langle i_{\text{PD}}\rangle$. The rectangular pulse shape simplified assumption is because of the dependence of the GR noise variance to the square of instantaneous photocurrent according to (33), in contrast to shot noise variance that is proportional to the instantaneous photocurrent. This square dependence consequently leads to the dependence of GR-noise PSD to the integral of the square of the normalized pulse shape. By assuming a rectangular pulse shape, we want to avoid such complications. For simplicity, we also assume that the pulsewidth is sufficiently longer than the decay time τ such that the GR stochastic properties do not vary during the presence of photocurrent. With these assumptions, the GR noise can be treated similar to the procedure the shot noise was treated in Section III-A and can be written as the product of Gaussian noise and a rectangular window function

$$i_{\text{GR}}(t) = i_{\text{GR-CW}}(t)\Pi(t) \tag{34}$$

where $i_{\text{GR}}(t)$ is the GR noise of the photodiode with pulsed stimulation, $i_{\text{GR-CW}}(t)$ is the GR noise of the photodiode stimulated with a CW optical field according to (33), which generates a photocurrent of $\langle i_{\text{PD}}\rangle/\gamma$, and $\Pi(t)$ is a periodic rectangular window function with a duty cycle of γ

$$\Pi(t) = \begin{cases} 1, & \text{for } T_{\text{rep}}(m-0.5\gamma) < t < T_{\text{rep}}(m+0.5\gamma) \\ 0, & \text{elsewhere} \end{cases} \tag{35}$$

where T_{rep} is the period of the rectangular pulse train and m is any integer. If we assume that the GR noise has a white spectrum compared to the frequency spectrum of the window

function ($\tau \ll \gamma T_{\text{rep}}$), the PSD and the autocorrelation function of the continuous-wave GR noise can be approximated as

$$S_{i_{\text{GR-CW}}}(f) \approx 2\langle i_{\text{PD}}\rangle^2 \tau/\gamma^2 n_0 \tag{36}$$

and

$$R_{i_{\text{GR-CW}}}(t,t') \approx 2\langle i_{\text{PD}}\rangle^2 \tau \delta(t-t')/\gamma^2 n_0. \tag{37}$$

The two-sided PSD of the GR noise can now be found similar to the procedure used in (27) and (28) as

$$\begin{aligned} S_{i_{\text{GR}}}(f) &= \lim_{T\to\infty} \frac{1}{2T}\int_{-T}^{+T}\int_{-T}^{+T} dt dt' \text{E}[i_{\text{GR}}(t) i_{\text{GR}}(t')] e^{j\omega(t-t')} \\ &= 2\langle i_{\text{PD}}\rangle^2 \tau/\gamma\, n_0. \end{aligned} \tag{38}$$

Therefore, for the same average photocurrent, the PSD of GR noise is inversely proportional to the duty cycle. We have to emphasize that the formalism above draws a qualitative picture of the effect of the duty cycle on the overall GR noise but is not very accurate for the stimulation of photodiodes with high-energy femtosecond pulses. For instance, the assumption of uniform electric field along the intrinsic region of photodiode used in derivation of (33) is no longer valid due to Coulomb interaction between charge carriers and space-charge effects [18], [19], [35]. Also, the photocurrent does not have a rectangular shape, and its rise/fall time considering the space-charge effect under the illumination of a photodiode with high-energy femtosecond optical pulses has to be taken into account.

Enhancement of GR noise under excitation of a photodiode with high optical intensities can also be observed by experiment. Fig. 5(a) shows a setup for photodiode noise measurement. An InGaAs photodiode with an active area diameter of 120 μm is illuminated with femtosecond pulses of an MLL (MENHIR1550 [37]), and an optical attenuator is used to change the intensity of the optical pulses. The optical pulses have a width of 185 fs and a repetition rate of 250 MHz. The photodiode is terminated to a 1-kΩ resistive load and connected to an FFT analyzer (Anapico APPH20G). The FFT analyzer has an input resistance of 1 kΩ (ac coupled), which makes the overall photodiode load resistance equal to 500 Ω. The 1-dB cutoff frequency of the measurement setup is approximately 2 MHz. Fig. 5(b) shows the measured noise voltage in $\text{V}/\sqrt{\text{Hz}}$. It can be seen that, at high illumination intensities with femtosecond pulses, the GR noise becomes dominant and exceeds the shot noise. The PSD of the output noise at 0 dBm incident optical power has good matching with the estimated shot noise. At 10-dBm incident optical power, however, the noise voltage has increased approximately by a factor of 10, which corresponds to an increase of 100 in V^2/Hz. This increase in noise PSD is a signature of GR noise because of the proportionality of its PSD to the square of photocurrent, in contrast to shot noise PSD that is proportional to the photocurrent. The enhancement of photodiode noise consequently leads to degradation of the BOMPD phase noise according to (31). The GR noise can be mitigated by increasing the number of equilibrium charge carriers, n_0 in (33), for instance by increasing the illumination area of the photodiode.

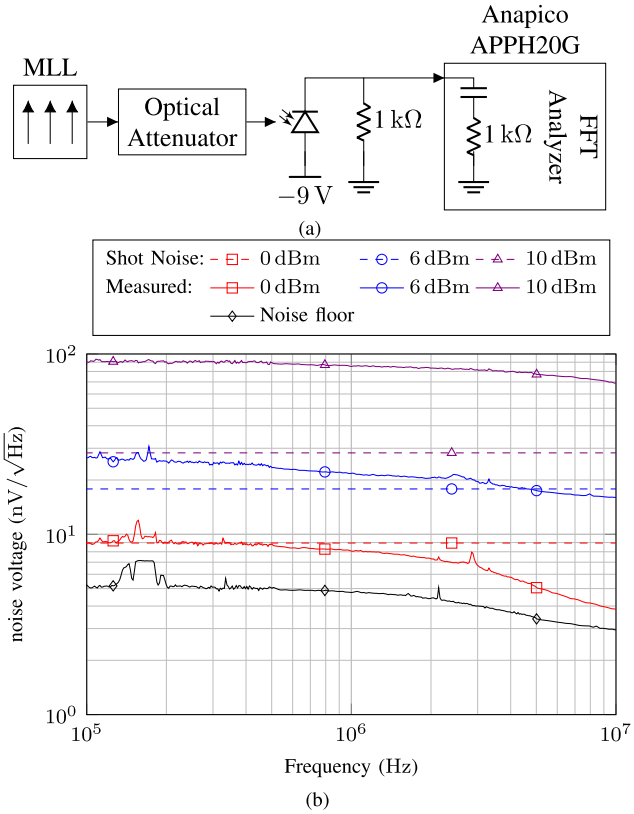

Fig. 5. (a) Photodiode noise measurement setup. (b) Photodiode (solid) measured noise PSD and (dashed) theoretical shot noise levels at different optical intensities; $v_n = (2qR_\lambda I_0)^{1/2} R_L$ ($\text{V}/\sqrt{\text{Hz}}$), where R_λ is the integrated responsivity taking into account its compression at high illumination levels according to (49), R_L is the effective load resistance (500 Ω), and I_0 is the average intensity of the optical beam.

The GR noise of photodiode is an undesired effect that has to be suppressed for low-phase-noise OEPLL designs. Due to the nonlinear dependence of photodiode response time to the optical intensity under pulsed excitation and also to the illumination condition, providing an exact formula for GR noise is complicated. The objective of the discussion above is to point to a strong source of noise in photodiodes when illuminated with high-energy pulses that lead to phase noise degradation in the BOMPD and discuss the available means to suppress this undesired noise.

C. Relative Intensity Noise of the MLL

The RIN is the intensity fluctuations of the light. RIN is associated with the light source, in contrast to shot noise that is due to the quantum nature of light itself. While shot noise is generated during the detection process, the noise of the laser is rooted in the generation of the light and can be modeled as an amplitude noise term in the intensity of the MLL beam [38] as

$$I(t) = I_0 T_{\text{ref}}\big[1 + a_n(t)\big] \sum_{m=-\infty}^{+\infty} P\left(t - \frac{m}{f_{\text{ref}}}\right) \tag{39}$$

where $a_n(t)$ is the RIN of the optical pulse train. Now, we investigate the effect of RIN of MLL on the noise performance of the BOMPD. The output currents of the photodiodes

incorporating the RIN of the laser (under the OEPLL-locked condition) can be written similar to (19) as

$$i_{\mathrm{PD}}^{\pm} = \frac{1}{2} R_\lambda I_0 T_{\mathrm{ref}} \big[1 + a_n(t)\big] \sum_{m=-\infty}^{+\infty} h\left(t - \frac{m}{f_{\mathrm{ref}}}\right). \quad (40)$$

The RIN of the laser generates noise current in both the upper and lower photodiodes. Unlike the shot noise of the photodiodes, these noise currents in the upper and lower photodiodes are perfectly correlated and cancel out when the OEPLL is in the steady state, $i_{\mathrm{PD}}^{+} = i_{\mathrm{PD}}^{-}$. Therefore, the noise of the laser does not have any first-order effect on the phase noise of the BOMPD.

D. Noise of MZM Bias Voltage

Another source of noise in the BOMPD is the low-frequency noise of the dc voltage used to bias the modulator. The noise of dc voltage, $v_n(t)$, can be incorporated in (2) as

$$\psi = \psi_{\mathrm{RF}} + \psi_{\mathrm{dc}} + \psi_n(t) \quad (41)$$

where

$$\psi_n(t) = \pi v_n(t) / V_{\pi,\mathrm{dc}}. \quad (42)$$

Assuming the linear photodiode model of Fig. 2(a), the output current of the BOMPD can be rewritten using (1) as

$$\begin{aligned} i_{\mathrm{BOMPD}} &= R_\lambda \big[I(t) \sin(\psi) \big] * h(t) \\ &\approx R_\lambda \big[I(t) \sin(\psi_{\mathrm{RF}} + \psi_{\mathrm{dc}}) \\ &\quad + \psi_n(t) I(t) \cos(\psi_{\mathrm{RF}} + \psi_{\mathrm{dc}}) \big] * h(t) \end{aligned} \quad (43)$$

where we assumed that $v_n(t)$ is small enough to have

$$\cos\big(\psi_n(t)\big) \approx 1 \quad \text{and} \quad \sin\big(\psi_n(t)\big) \approx \psi_n(t). \quad (44)$$

The first term in the brackets on the right-hand side of (43) leads to the phase detector characteristic function. The second term is the noise of the bias voltage and shows that the bias voltage noise is multiplied by the intensity waveform of the MLL $I(t)$ and, due to its harmonious nature, is modulated around integer multiples of the reference repetition rate. These modulated noise terms are filtered by the loop filter, and only the low-frequency noise term around zero frequency affects the BOMPD output noise current. The low-frequency term of this noise current can be found similar to the treatment of the phase detector characteristic curves in [30], and the detailed steps are given in Appendix A. The relation between the BOMPD noise current due to the bias voltage of the dc electrode, $i_{n,\mathrm{bias}}$, and the noise of the dc voltage is

$$i_{n,\mathrm{bias}}(t) = R_\lambda I_0 \cos(\psi_0) \psi_n(t) \quad (45)$$

where ψ_0 is given in (9) and is zero at the steady state. Therefore, the output noise current at the steady state simply will be

$$i_{n,\mathrm{bias}}(t) = R_\lambda I_0 \psi_n(t). \quad (46)$$

The PSD of this noise current can be found by substituting (42) into (46)

$$S_{i_{n,\mathrm{bias}}}(f) = \left(\frac{\pi R_\lambda I_0}{V_{\pi,\mathrm{dc}}}\right)^2 S_{v_n}(f) \quad (47)$$

where $S_{v_n}(f)$ is the PSD of v_n. The contribution of the bias voltage noise to the overall phase noise can then be found by substituting the PSD of this noise current into (14)

$$S_{\phi_{n,\mathrm{bias}}}(f) = \frac{\pi^2}{V_{\pi,\mathrm{dc}}^2 \left(\alpha^2 - \psi_{\mathrm{dc}}^2\right)} S_{v_n}(f). \quad (48)$$

This equation shows that the phase noise caused by the noise of the bias voltage is independent of the average optical excitation level and the photodiode responsivity. This leaves the designer with a few degrees of freedom to suppress the noise caused by the bias voltage: using a modulator with higher π-voltage for the dc-electrode, increasing the RF power level and, consequently α, and also using a dc source with lower noise levels in the first place. Since the phase noise caused by photodiodes' shot noise is inversely proportional to the average intensity of the optical beam according to (31), it is necessary to reduce the noise of the bias voltage to make sure that the OEPLL phase noise is not limited by the noise of the bias voltage.

IV. Nonlinear Effects in BOMPD

Extracting the phase information of a periodic signal requires a nonlinear operation, which makes any phase detector a nonlinear device. Although such a device is nonlinear, it behaves linearly in the phase domain. Therefore, by nonlinearity in BOMPD, we address the mechanisms that affect the phase detector characteristic function beyond the scope of the linear phase detector model. These mechanisms are a function of the excitation levels of the inputs of the BOMPD: the intensity of the optical field and the RF excitation amplitude. With respect to the optical input, we assume that BIM behaves linearly and limit the discussion in Section IV-A to nonlinearity in photodiodes. The nonlinear effects on the BOMPD characteristic function with respect to the RF excitation amplitude are discussed in Section IV-B.

A. Saturation of the Photodiodes

High-energy pulses of MLLs affect the performance of photodiodes with space-charge effect and absorption saturation [18], [19], [20], [21], [39]. The space-charge effect leads to a counteracting E-field in the illumination region of the photodiode, which slows down the charge carriers and increases the transit time. This effect is especially important for high-speed and high-power photodetectors used for the generation of RF signals with high signal-to-noise ratios (SNRs). The increase in the response time due to the space-charge effect is not problematic in the BOMPD since the OEPLL loop is much slower than the photocurrent pulses. Therefore, the approximation of $H(f) \approx 1$ is still valid ($H(f)$ models the transit-time spread of the photodiode, as discussed in Section III-A).

High-energy pulses of MLLs also lead to saturation of charge carriers in the active region of the photodiode and compression of its responsivity. This mechanism is especially important in the BOMPD, as the phase detection gain is directly proportional to the photodiode responsivity. The linear BOMPD gain formula in (10) suggests that increasing the

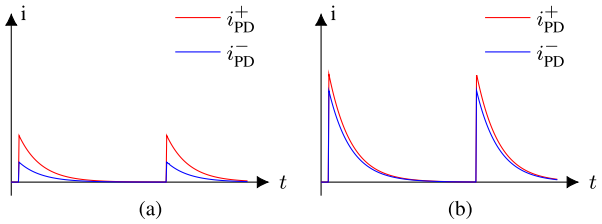

Fig. 6. Qualitative illustration of the upper (red) and lower (blue) photodiode currents of the BOMPD in the presence of a small phase difference ϕ when the intensity of the input beam (a) is low and the photodiodes operate in the linear region and (b) is high and the photodiodes operate in the saturation region.

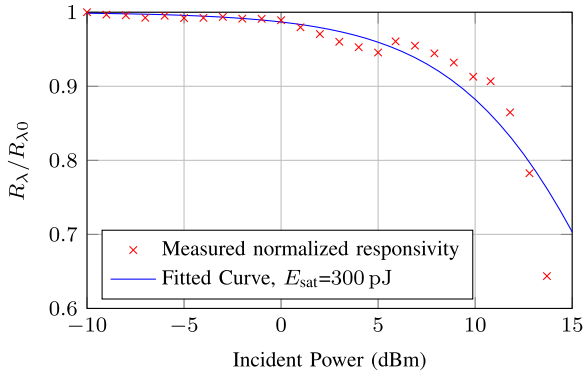

Fig. 7. Red: measured normalized integrated responsivity. Blue: fit curve according to (49).

intensity of the optical field results in more phase detector gain; however, absorption saturation of the photodiodes puts a limit on the gain enhancement. This is illustrated graphically in Fig. 6(a) and (b), and the photocurrent pulses of the photodiode pair in the presence of a small phase difference ϕ for different optical excitation levels are drawn. Although the photocurrent pulses in Fig. 6(a) have a smaller amplitude than that of the photocurrent pulses in Fig. 6(b), they exhibit a higher average current difference as the photodiodes are still in the linear region. This current difference is an indication of the BOMPD phase detection gain. In other words, at very high optical pulse energies, the upper and lower photodiodes get saturated and generate almost equal photocurrents, which leads to lower phase detection gain.

The absorption saturation of photodiodes has been modeled in [39] by defining *integrated responsivity* as a function of the pulse energy

$$R_\lambda(E) = \frac{R_{\lambda 0}}{1 + E/E_{\text{sat}}} \tag{49}$$

where E is the pulse energy, $R_{\lambda 0}$ is the linear responsivity, and E_{sat} is the pulse energy at which the integrated responsivity is reduced by a factor of 2. It is noteworthy that this model for saturation of semiconductors is similar to the model of a fast saturable absorber. However, instead of dependence on the instantaneous intensity of the optical pulse, the responsivity is a function of the pulse energy. The measured integrated responsivity of a commercial InGaAs photodiode with an active area diameter of 120 μm is shown in Fig. 7. A commercial MLL with a center wavelength of 1560 nm and a pulsewidth of 185 fs is used for the characterization.

In order to formulate the effect of the absorption saturation on the BOMPD gain, the photocurrent of upper and lower photodiodes as a function of the pulse energy is derived. The average of the difference of these photocurrent pulses is the BOMPD gain according to (6). The energy of the output optical pulses of the BOMPD can be found using (4) and (15) as

$$E_y^{\pm} = \frac{1}{2} I_0 T_{\text{ref}} \left[1 \pm \sin(\psi_0)\right] \tag{50}$$

where ψ_0 is given in (9). Using the nonlinear responsivity in (49), the output currents of the photodiodes can be found similar to (17) as

$$i_{\text{PD}}^{\pm} = \frac{1}{2} I_0 T_{\text{ref}} R_\lambda\left(E_y^{\pm}\right)\left[1 \pm \sin(\psi_0)\right] \sum_{m=-\infty}^{+\infty} h\left(E_y^{\pm}, t - \frac{m}{f_{\text{ref}}}\right) \tag{51}$$

where we replaced the linear impulse response $h(t)$ with nonlinear $h(E, t)$ and the linear responsivity R_λ with $R_\lambda(E)$, which are functions of the optical pulse energy. The normalization condition in (16) still holds for the nonlinear response since the compression of the responsivity due to absorption saturation is already included in (49). The average photodiode currents, therefore, are

$$\left\langle i_{\text{PD}}^{\pm} \right\rangle = \frac{1}{2} I_0 R_\lambda\left(E_y^{\pm}\right)\left[1 \pm \sin(\psi_0)\right]. \tag{52}$$

The BOMPD characteristic function can be found using equations (6) and (52) and is plotted for pulse energies close to saturation of photodiodes in Fig. 8(a). It can be seen that the slope of the characteristic function at the zero crossing decreases for high pulse energies, which is also shown qualitatively using Fig. (6). The phase detector characteristic function and gain have complicated forms when described with respect to the phase difference ϕ. However, the phase detector gain K_ϕ at the zero crossing has a simple expression (the derivation steps are given in Appendix B)

$$K_\phi = \frac{R_{\lambda 0} I_0 \sqrt{\alpha^2 - \psi_{\text{dc}}^2}}{\left(1 + I_0 T_{\text{ref}}/2E_{\text{sat}}\right)^2} \tag{53}$$

and is plotted in Fig. 8(b). The numerator in (53) is the same as the linear phase detector gain in (10), and for very low pulse energies, $I_0 \ll 2 f_{\text{ref}} E_{\text{sat}}$, the denominator converges to 1. At very high pulse energies, the phase detector gain becomes inversely proportional to the intensity of the optical beam. The maximum of phase detector gain is

$$K_{\phi,\max} = \frac{R_{\lambda 0} E_{\text{sat}}}{2T_{\text{ref}}} \sqrt{\alpha^2 - \psi_{\text{dc}}^2} \tag{54}$$

which occurs at the average optical intensity of

$$I_0 = 2E_{\text{sat}}/T_{\text{ref}}. \tag{55}$$

This decrease in the BOMPD gain due to high-energy pulses has an adverse effect on the phase noise according to (31). In addition to gain deterioration, high-energy optical pulses of MLL increase the GR noise of the photodiodes. The GR noise variance of the photodiode is proportional to the square of the photocurrent and exceeds the shot noise at high illumination

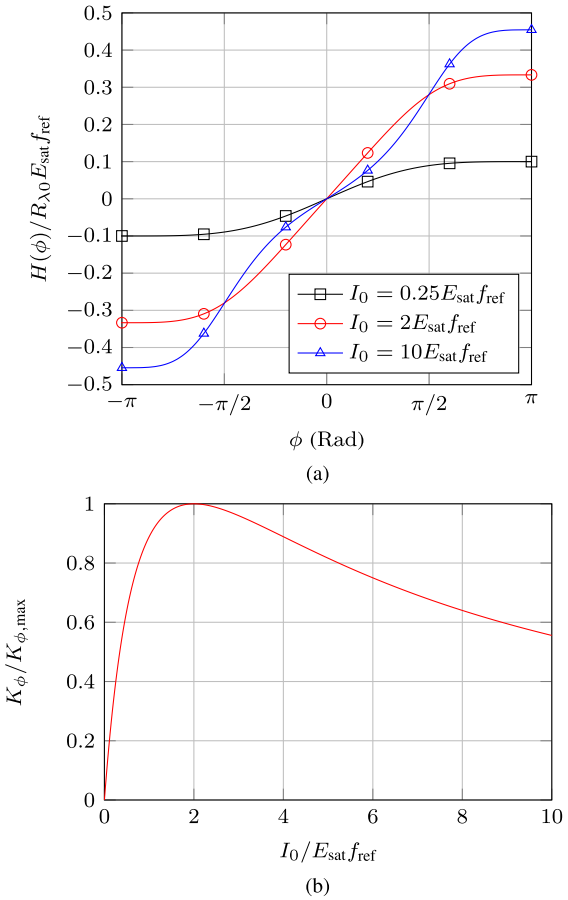

Fig. 8. (a) Characteristic function of BOMPD at different optical pulse energy levels corresponding to (black) linear region, (red) maximum phase detector gain, and (blue) deep saturation of photodiodes. (b) Normalized gain of BOMPD with respect to input average optical intensity.

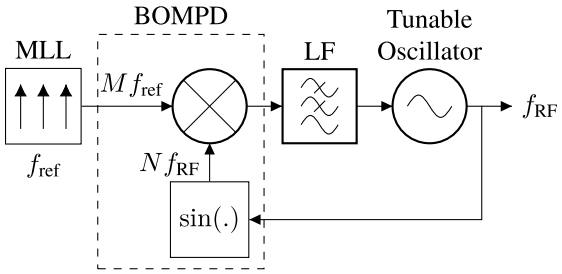

Fig. 9. Block diagram of OEPLL with the nonlinear model of BOMPD.

levels, as discussed in Section III-B. Degradation of phase detector gain and enhancement of GR noise due to high-energy pulses have an adverse effect on the BOMPD phase noise, and for low-phase-noise OEPLL, operating the BOMPD in this operating region should be avoided.

B. RF Nonlinearity in BOMPD and Interharmonic Locking

Another nonlinear effect in the BOMPD is the intrinsic nonlinear properties of the BIM characteristic function. The RF voltage v_{RF} goes under a nonlinear transformation in the BOMPD due to $\sin(\psi)$ term in (1). This nonlinear transformation leads to the internal generation of harmonics of the RF signal, which can be used for locking on interharmonics (noninteger harmonics) of the reference repetition rate [29]. This nonlinear behavior is illustrated in the OEPLL block diagram in Fig. 9 where the BOMPD is modeled with an ideal balanced frequency mixer and a nonlinear block sin(.). The envelope of the MLL output contains integer multiples of its repetition rate Mf_{ref} and the output of sin(.) block contains integer multiples of the RF signal frequency Nf_{RF}. The necessary (but not sufficient) condition for phase locking is that these frequencies are equal

$$f_{\text{RF}} = \frac{M}{N} f_{\text{ref}}. \tag{56}$$

This operating mode of OEPLL is called N'th-order interharmonic locking. The N'th-order characteristic functions of the BOMPD, $H_N(\phi)$, have been derived in [29] and, for $n = 2$ and 4, have a simple closed form

$$H_2(\phi) = R_\lambda I_0 \sin(\psi_{\text{dc}}) \cos[\alpha \sin(\phi)] \tag{57}$$

and

$$H_4(\phi) = \frac{1}{2} R_\lambda I_0 \sin(\psi_{\text{dc}})[\cos(\alpha \sin(\phi)) + \cos(\alpha \cos(\phi))]. \tag{58}$$

The term $\sin(\psi)$ in the characteristic function of MZM in (1) has odd symmetry around $\psi_{\text{dc}} = 0$ and even symmetry around $\psi_{\text{dc}} = \pi/2$ with respect to v_{RF}. Therefore, only odd harmonics of a sinusoidal RF signal are generated at $\psi_{\text{dc}} = 0$. This explains the proportionality of the second- and fourth-order characteristic functions to $\sin(\psi_{\text{dc}})$. The BOMPD characteristic curves for different values of α are plotted in Fig. 10(a)–(c), respectively. The second- and fourth-order characteristic curves do not have a zero crossing for all RF excitation amplitudes, which is necessary for type II PLLs [30]. A zero crossing can be guaranteed by proper selection of α such that the BOMPD characteristic function has a zero average. The average value of the BOMPD characteristic function is

$$\langle H_N(\phi) \rangle_\phi = R I_0 \sin(\psi_{\text{dc}}) J_0(\alpha) \tag{59}$$

where $\langle . \rangle_\phi$ denotes averaging with respect to variable ϕ and J_0 denotes the Bessel function of the first kind of order 0. Therefore, with an α equal to the first zero of J_0, a zero-crossing in the characteristics function can be guaranteed.

V. System-Level Simulation, Implementation, and Measurement Results

Fig. 11(a) shows the detailed block diagram of the OEPLL. The optical reference is an MLL from MENHIR photonics with a center wavelength of 1560 nm and a repetition rate of 250 MHz [37]. The BOMPD is realized using a balanced lithium niobate ($LiNbO_3$) MZM, which has two separate electrodes for RF modulation and dc bias. A polarization controller matches the polarization of the MLL output with the polarization required at the MZM input. A pair of InGaAs photodiodes with an active area diameter of 120 μm converts the optical outputs of the MZM to an electrical current. The optical power budget is set such that each photodiode receives 1 mW without RF stimulation of the MZM. The BOMPD current pulses are integrated via a series-RC loop filter, similar to type II charge pump PLLs. An yttrium–iron–garnet (YIG)

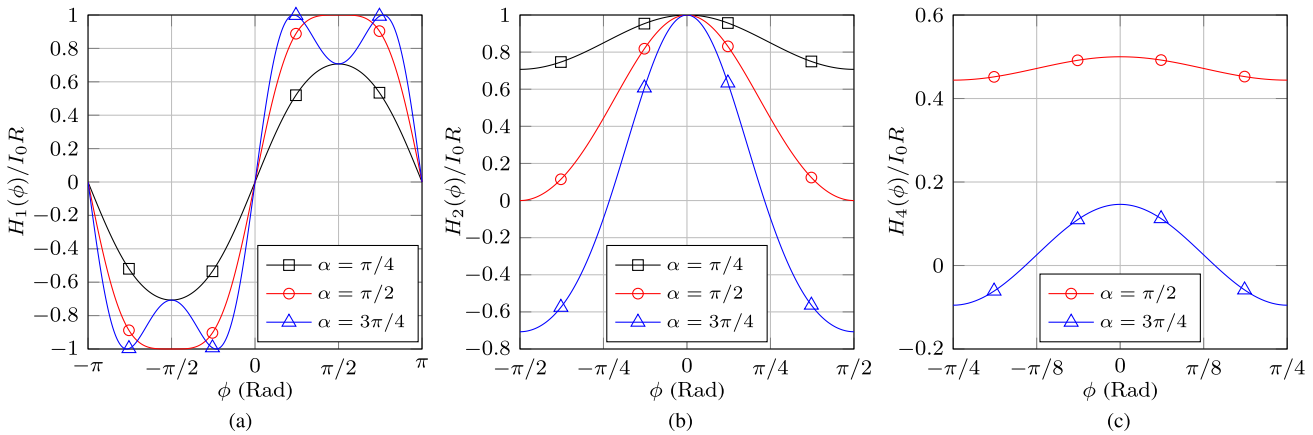

Fig. 10. BOMPD characteristic curves for (a) harmonic locking at $\psi_{\rm dc} = 0$, (b) second-order interharmonic locking at $\psi_{\rm dc} = \pi/2$, and (c) fourth-order interharmonic locking at $\psi_{\rm dc} = \pi/2$ for different RF amplitudes: black: $\alpha = \pi/4$; red: $\alpha = \pi/2$; and blue: $\alpha = 3\pi/4$.

oscillator with a frequency range of 2–20 GHz is used as a tunable oscillator. The main coil of the YIG oscillator is used for coarse tuning of the frequency, and the FM coil is used for phase locking. Two low-noise digital-to-analog converters (DACs) set the voltage of the dc electrode of the MZM and the current of the main coil of the YIG oscillator.

In order to estimate the overall phase noise, the OEPLL and its noise sources are modeled in the phase domain, as illustrated in Fig. 11(b). The transfer functions of these noise sources are found using the linear-control-theory toolbox. The open-loop transfer function is defined as the product of the transfer functions of loop components

$$H_{\rm OL}(s) := K_\phi H_{\rm LF}(s)\frac{K_{\rm I}}{s} \tag{60}$$

where $H_{\rm LF}(s)$ is the overall transfer function of the loop filter & YIG oscillator driver, and $K_{\rm I}$ is the tuning sensitivity of the YIG oscillator. With this definition, the transfer functions of the OEPLL noise sources can be written as

$$H_{\rm R}(s) = \frac{\Phi_{\rm out}}{\Phi_{n,{\rm R}}}(s) = M\frac{H_{\rm OL}(s)}{1+H_{\rm OL}(s)} \tag{61a}$$

$$H_{\rm BOMPD}(s) = \frac{\Phi_{\rm out}}{\Phi_{n,{\rm BOMPD}}}(s) = \frac{H_{\rm OL}(s)}{1+H_{\rm OL}(s)} \tag{61b}$$

$$H_{\rm TO}(s) = \frac{\Phi_{\rm out}}{\Phi_{n,{\rm TO}}}(s) = \frac{1}{1+H_{\rm OL}(s)}. \tag{61c}$$

Equations (61a) and (61b) show that the phase noise of the reference and the BOMPD are shaped similarly. Due to natural pole of the oscillator at 0 Hz, the loop filter has an infinite gain at 0 Hz. Therefore, the phase noise of the reference is transferred to the output with a gain equal to the harmonic number, M. The phase detector transfer function *shape* is similar but is insensitive to the harmonic number. The tunable oscillator noise transfer function is complementary to that of the reference and phase detector. Therefore, the noise of the tunable oscillator is suppressed inside the loop bandwidth and dominates outside of it.

The overall phase noise PSD is the geometrical sum of these different noise sources multiplied by their transfer function in the Fourier domain. Therefore,

$$\begin{aligned} S_{\phi_{n,{\rm out}}}(f) = {} & S_{\phi_{n,{\rm R}}}(f)|H_{\rm R}(j2\pi f)|^2 \\ & + S_{\phi_{n,{\rm BOMPD}}}(f)|H_{\rm BOMPD}(j2\pi f)|^2 \\ & + S_{\phi_{n,{\rm TO}}}(f)|H_{\rm TO}(j2\pi f)|^2. \end{aligned} \tag{62}$$

The phase noise of the reference and the YIG oscillator has been provided by the manufacturer and were used for overall phase noise estimation. The BOMPD phase noise has been calculated according to (31).

Fig. 11(c) shows the open-loop phase noise of OEPLL components and the estimated closed-loop phase noise at 10 GHz. At low offset frequencies (approximately below 50 kHz), the phase noise is dominated by the reference MLL. At high offset frequencies (approximately above 3 MHz), the phase noise is dominated by the tunable oscillator. It is in the intermediate offset frequency range that the BOMPD (or, in general, any phase detector in various types of PLLs) plays a significant role.

The phase noise measurement results for the harmonic locking scenario are plotted in Fig. 11(d). The loop filter has been optimized for the carrier frequency of 10 GHz, and the OEPLL shows the best performance at this frequency with an in-band phase noise of -150 dBc/Hz. The measurement results for second- and fourth-order interharmonic lockings are shown in Fig. 11(e). Compared to the harmonic-locking scenario, the in-band phase noise has increased by approximately a factor of 10, and the loop bandwidth is also reduced. This is due to lower BOMPD gain K_ϕ at interharmonic frequencies, which can also be observed in Fig. 10(a)–(c) as the slope of the characteristic function at the zero crossing. Further increase in the optical power increases the phase detector gain and the loop bandwidth. However, with 1 mW of the optical power at the photodiodes, the photodiodes are operating in the close-to-GR-noise dominating regime, and no phase noise enhancement has been observed by increasing the optical power budget.

Fig. 11(f) compares this work with the state-of-the-art OEPLLs and commercial signal generators for a carrier frequency of 10 GHz [17], [40], [41]. Compared to the OEPLL published by Jung *et al.* [17], this OEPLL has similar in-band phase noise performance at intermediate offset frequencies. Outside the loop bandwidth, Jung *et al.* [17] have better phase noise since a DRO has been used as the tunable oscillator; the extremely low-frequency range of DRO, however, makes the OEPLL reported by Jung *et al.* [17] capable of

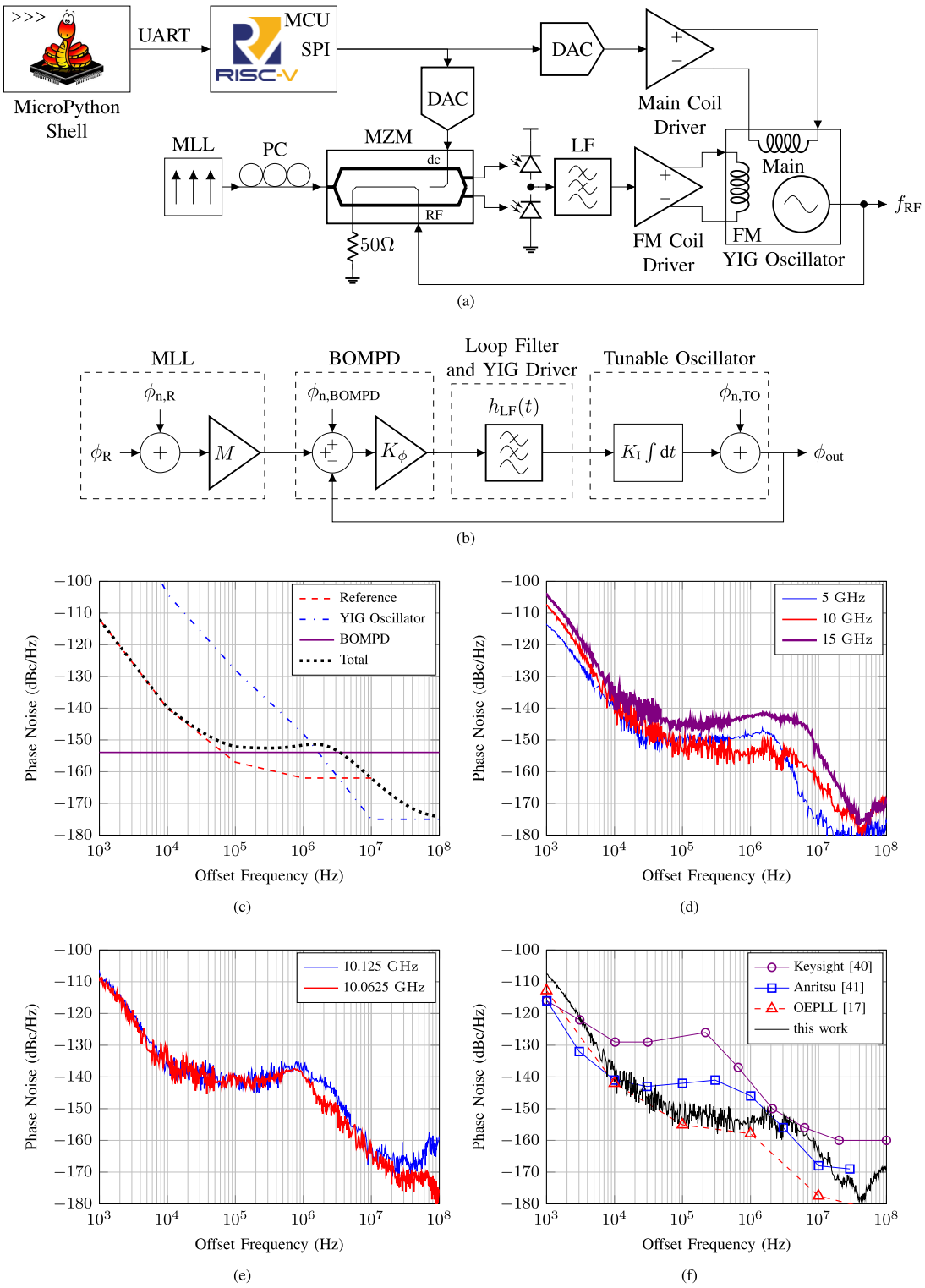

Fig. 11. (a) Optoelectronic PLL using BOMPD. (b) Linear model of OEPLL in the phase domain. (c) Phase noise simulation for 10-GHz carrier frequency. (d) Measured phase noise at harmonic frequencies. (e) Measured phase noise at interharmonic frequencies. (f) Comparison of this work with state of the art at 10-GHz carrier frequency. MCU; microcontroller unit. DAC: digital-to-analog converter. MLL: mode-locked laser. MZM: Mach–Zehnder modulator. PC: polarization controller. LF: loop filter. YIG: yttrium iron garnet.

generating only one single frequency. The OEPLL shows its superior performance especially compared to commercial signal generators. At offset frequencies between approximately 10 kHz and 1 MHz, the phase noise of this work is better than that of Keysight and Anritsu signal generators by almost 20 and 10 dB, respectively. The phase noise of this work at close-in carrier offset frequencies is higher than that of the state-of-the-art signal generators and the OEPLL reported in [17]. This is due to the higher phase noise of the reference MLL at low offset frequencies. The phase noise at close-in offset frequencies can be improved by various techniques, such as locking the repetition rate of MLL on a quartz

reference, or employing a more sophisticated optical frequency division (OFD) scheme [15], [16], or using a different class of MLLs with better linewidth, such as the one reported in [42] and [43].

VI. Conclusion

This article provides a detailed analysis of the OEPLL using a BOMPD. The effects of different noise sources on the OEPLL, such as shot noise and GR noise of photodiodes, RIN of MLL, and the noise of the dc voltage applied to the intensity modulator are modeled. In addition, different nonlinear mechanisms with respect to optical and RF inputs of the BOMPD that affect its performance are discussed. An operating mode of OEPLL that can be used to lock on interharmonics of the MLL repetition rate due to the inherent nonlinear behavior of the intensity modulator is demonstrated. This detailed analysis paves the way for ultralow-noise frequency synthesis based on optical clock sources. As an example, an OEPLL is presented which can lock on 40'th, 40(1/2), and 40(1/4) harmonics of the reference repetition rate. The in-band phase noise of the OEPLL at 100-kHz offset frequency is below −150 dBc/Hz for a carrier frequency of 10 GHz, which is more than 10 dB below that of state-of-the-art commercial frequency synthesizers.

Appendix A
Transfer Characteristic of the Bias Electrode Noise

The noise of the dc voltage applied to the dc electrode of the modulator is included in (41), and the modulator output considering this noise voltage is given by (43). The noise term in (43) is

$$i_{n,\text{bias}}(t) = R_\lambda\big[\psi_n(t) I(t)\cos(\psi_{\text{RF}}(t)+\psi_{\text{dc}})\big] * h(t) \quad (63)$$

where $i_{n,\text{bias}}$ denotes the noise term of the output current of the BOMPD. The term in brackets shows that $\psi_n(t)$ is modulated by the modulation term (MT)

$$\text{MT} = I(t)\cos(\psi_{\text{RF}}(t)+\psi_{\text{dc}}) \quad (64)$$

which has many tones. For the phase detector application, only the dc term of MT is important, and the higher order harmonics are filtered by the loop filter. This dc term can be written as

$$\langle \text{MT}\rangle = \left\langle I_0 T_{\text{ref}} \sum_{m=-\infty}^{+\infty} \delta\left(t - \frac{m}{f_{\text{ref}}}\right)\cos(\psi_{\text{RF}}(t)+\psi_{\text{dc}})\right\rangle \quad (65)$$

where we used (3) and approximated the optical pulse shape as the Dirac delta function. Assuming a single tone excitation of the RF electrode with (5) and applying the harmonic locking condition $\omega_{\text{RF}} = N\omega_{\text{ref}}$, the optical pulse samples the RF signal at the same phase in every cycle of the RF signal. Therefore, the average of the modulation term can be found by averaging over the first cycle of the optical pulse as

$$\langle \text{MT}\rangle = I_0\cos(\psi_0) \quad (66)$$

where ψ_0 is given in (9). Therefore, with an approximation of neglecting the high-frequency terms of (63), the output noise of the BOMPD can be written as

$$i_{n,\text{bias}}(t) \approx R_\lambda I_0\cos(\psi_0)\psi_n(t) * h(t). \quad (67)$$

Finally, taking into account the locking condition $\psi_0 = 0$ and assuming that the photodiode bandwidth is much higher than the bandwidth of the voltage noise applied to the dc electrode, $h(t)$ can be approximated as the Dirac delta function, and (67) can be further simplified to (46).

Appendix B
Gain of BOMPD With Nonlinear Photodiode

The phase detector characteristic function is given by (6), and the phase detector gain is the slope of the characteristic function at the zero crossing

$$\begin{aligned} K_\phi &= \frac{d}{d\phi}\langle i_{\text{PD}}^+ - i_{\text{PD}}^-\rangle\Big|_{\psi_0=0} \\ &= \frac{d}{d\phi}\langle i_{\text{PD}}^+\rangle\Big|_{\psi_0=0} - \frac{d}{d\phi}\langle i_{\text{PD}}^-\rangle\Big|_{\psi_0=0} \end{aligned} \quad (68)$$

where $\langle i_{\text{PD}}^\pm\rangle$ is given by (52). Now, we find the derivative of $\langle i_{\text{PD}}^\pm\rangle$ with respect to ϕ

$$\frac{d}{d\phi}\langle i_{\text{PD}}^\pm\rangle = \frac{d}{d\phi}\left[\frac{R_{\lambda 0} I_0\big[1\pm\sin(\psi_0)\big]}{2 + I_0 T_{\text{ref}}\big[1\pm\sin(\psi_0)\big]/E_{\text{sat}}}\right] \quad (69)$$

where we substituted (49) and (50) into (52). The derivative of $\langle i_{\text{PD}}^\pm\rangle$ with respect to ϕ can be found using the chain rule and (9) as

$$\begin{aligned} \frac{d}{d\phi}\langle i_{\text{PD}}^\pm\rangle &= \frac{d\psi_0}{d\phi}\frac{d}{d\psi_0}\left[\frac{R_{\lambda 0} I_0\big[1\pm\sin(\psi_0)\big]}{2 + I_0 T_{\text{ref}}\big[1\pm\sin(\psi_0)\big]/E_{\text{sat}}}\right] \\ &= \frac{\pm 2\alpha\cos(\phi)\cos(\psi_0) R_{\lambda 0} I_0\big[1\pm\sin(\psi_0)\big]}{\big(2 + I_0 T_{\text{ref}}\big[1\pm\sin(\psi_0)\big]/E_{\text{sat}}\big)^2}. \end{aligned} \quad (70)$$

Imposing the zero crossing condition, $\psi_0 = 0$, on (70) gives

$$\frac{d}{d\phi}\langle i_{\text{PD}}^\pm\rangle\Big|_{\psi_0=0} = \frac{\pm R_{\lambda 0} I_0\sqrt{\alpha^2 - \psi_{\text{dc}}^2}}{2(1 + I_0 T_{\text{ref}}/2E_{\text{sat}})^2}. \quad (71)$$

Substituting (71) into (68) gives the phase detector gain in (53).

References

[1] T. Udem, R. Holzwarth, and T. W. Hänsch, "Optical frequency metrology," *Nature*, vol. 416, no. 6877, pp. 233–237, Mar. 2002.

[2] T. Udem, J. Reichert, R. Holzwarth, and T. W. Hänsch, "Accurate measurement of large optical frequency differences with a mode-locked laser," *Opt. Lett.*, vol. 24, no. 13, p. 881, Jul. 1999.

[3] J. Reichert, R. Holzwarth, T. Udem, and T. W. Hänsch, "Measuring the frequency of light with mode-locked lasers," *Opt. Commun.*, vol. 172, nos. 1–6, pp. 59–68, Dec. 1999.

[4] I. Coddington, W. C. Swann, and N. R. Newbury, "Coherent dual-comb spectroscopy at high signal-to-noise ratio," *Phys. Rev. A, Gen. Phys.*, vol. 82, no. 4, Oct. 2010, Art. no. 043817.

[5] B. Bernhardt *et al.*, "Cavity-enhanced dual-comb spectroscopy," *Nature Photon.*, vol. 4, no. 1, pp. 55–57, Jan. 2010.

[6] A. Cingöz *et al.*, "Direct frequency comb spectroscopy in the extreme ultraviolet," *Nature*, vol. 482, no. 7383, pp. 68–71, Feb. 2012.

[7] K. Krzempek, G. Dudzik, and K. Abramski, "Photothermal spectroscopy of CO_2 in an intracavity mode-locked fiber laser configuration," *Opt. Exp.*, vol. 26, no. 22, p. 28861, Oct. 2018.

[8] A. Khilo *et al.*, "Photonic ADC: Overcoming the bottleneck of electronic jitter," *Opt. Exp.*, vol. 20, no. 4, p. 4454, Feb. 2012.

[9] C. Deakin and Z. Liu, "Dual frequency comb assisted analog-to-digital conversion," *Opt. Lett.*, vol. 45, no. 1, p. 173, Dec. 2019.
[10] M. Hadjloum, M. El Gibari, H. Li, and A. S. Daryoush, "Leaky waveguide deflector for 40 GS/s and 6 bits all-optical analog-to-digital converters," *J. Franklin Inst.*, vol. 354, no. 18, pp. 8710–8720, Dec. 2017.
[11] P. Ghelfi, F. Scotti, A. T. Nguyen, G. Serafino, and A. Bogoni, "Novel architecture for a photonics-assisted radar transceiver based on a single mode-locking laser," *IEEE Photon. Technol. Lett.*, vol. 23, no. 10, pp. 639–641, May 15, 2011.
[12] P. Ghelfi, F. Scotti, F. Laghezza, and A. Bogoni, "Photonic generation of phase-modulated RF signals for pulse compression techniques in coherent radars," *J. Lightw. Technol.*, vol. 30, no. 11, pp. 1638–1644, Jun. 1, 2012.
[13] P. Ghelfi *et al.*, "A fully photonics-based coherent radar system," *Nature*, vol. 507, no. 7492, pp. 341–345, Mar. 2014.
[14] F. Quinlan *et al.*, "Ultralow phase noise microwave generation with an Er: Fiber-based optical frequency divider," *Opt. Lett.*, vol. 36, no. 16, p. 3260, Aug. 2011.
[15] X. Xie *et al.*, "Photonic microwave signals with zeptosecond-level absolute timing noise," *Nature Photon.*, vol. 11, no. 1, pp. 44–47, Nov. 2016.
[16] J. W. Zobel *et al.*, "Comparison of optical frequency comb and sapphire loaded cavity microwave oscillators," *IEEE Photon. Technol. Lett.*, vol. 31, no. 16, pp. 1323–1326, Aug. 15, 2019.
[17] K. Jung, J. Shin, and J. Kim, "Ultralow phase noise microwave generation from mode-locked Er-fiber lasers with subfemtosecond integrated timing jitter," *IEEE Photon. J.*, vol. 5, no. 3, Jun. 2013, Art. no. 5500906.
[18] P.-L. Liu, K. J. Williams, M. Y. Frankel, and R. D. Esman, "Saturation characteristics of fast photodetectors," *IEEE Trans. Microw. Theory Techn.*, vol. 47, no. 7, pp. 1297–1303, Jul. 1999.
[19] K. Williams, R. Esman, and M. Dagenais, "Effects of high space-charge fields on the response of microwave photodetectors," *IEEE Photon. Technol. Lett.*, vol. 6, no. 5, pp. 639–641, May 15, 1994.
[20] K. J. Williams and R. D. Esman, "Design considerations for high-current photodetectors," *J. Lightw. Technol.*, vol. 17, no. 8, pp. 1443–1454, Aug. 1, 1999.
[21] A. Beling, X. Xie, and J. C. Campbell, "High-power, high-linearity photodiodes," *Optica*, vol. 3, no. 3, p. 328, Mar. 2016.
[22] J. Kim, F. X. Kärtner, and M. H. Perrott, "Femtosecond synchronization of radio frequency signals with optical pulse trains," *Opt. Lett.*, vol. 29, no. 17, p. 2076, Sep. 2004.
[23] J. Kim, F. X. Kärtner, and F. Ludwig, "Balanced optical-microwave phase detectors for optoelectronic phase-locked loops," *Opt. Lett.*, vol. 31, no. 24, p. 3659, Nov. 2006.
[24] K. Jung and J. Kim, "Subfemtosecond synchronization of microwave oscillators with mode-locked Er-fiber lasers," *Opt. Lett.*, vol. 37, no. 14, p. 2958, Jul. 2012.
[25] K. Jung and J. Kim, "Long-term stable sub-femtosecond synchronization of microwave signals with mode-locked Er-fiber lasers," in *Proc. IEEE Int. Freq. Control Symp. Proc.*, May 2012, pp. 1–4.
[26] A. H. Nejadmalayeri and F. X. Kärtner, "Mach-zehnder based balanced optical microwave phase detector," in *Proc. Conf. Lasers Electro-Optics*, 2012, pp. 1–2.
[27] M. Bahmanian, J. Tiedau, C. Silberhorn, and J. C. Scheytt, "Octave-band microwave frequency synthesizer using mode-locked laser as a reference," in *Proc. Int. Topical Meeting Microw. Photon. (MWP)*, Oct. 2019, pp. 1–4.
[28] M. Bahmanian, S. Fard, B. Koppelmann, and J. C. Scheytt, "Ultra low phase noise and ultra wide-band frequency synthesizer using an optical clock source," in *IEEE MTT-S Int. Microw. Symp. Dig.*, Aug. 2020, pp. 1283–1286.
[29] M. Bahmanian, C. Kress, and J. C. Scheytt, "Locking of microwave oscillators on the interharmonics of mode-locked laser signals," *Opt. Exp.*, vol. 30, no. 5, pp. 7763–7771, Feb. 2022. [Online]. Available: http://opg.optica.org/oe/abstract.cfm?URI=oe-30-5-7763
[30] M. Bahmanian and J. C. Scheytt, "A 2–20-GHz ultralow phase noise signal source using a microwave oscillator locked to a mode-locked laser," *IEEE Trans. Microw. Theory Techn.*, vol. 69, no. 3, pp. 1635–1645, Mar. 2021.
[31] B. Razavi, *RF Microelectronics*. London, U.K.: Pearson, 2011.
[32] R. Loudon, *The Quantum Theory of Light*. Oxford, U.K.: Oxford Univ. Press, 2000.
[33] B. Saleh and M. Teich, *Fundamentals of Photonics* (Wiley Series in Pure and Applied Optics). Hoboken, NJ, USA: Wiley, 2007.
[34] F. Quinlan, T. M. Fortier, H. Jiang, and S. A. Diddams, "Analysis of shot noise in the detection of ultrashort optical pulse trains," *J. Opt. Soc. Amer. B, Opt. Phys.*, vol. 30, no. 6, p. 1775, May 2013.
[35] K. M. van Vliet, "Irreversible thermodynamics and carrier density fluctuations in semiconductors," *Phys. Rev.*, vol. 110, no. 1, pp. 50–61, Apr. 1958, doi: 10.1103/PhysRev.110.50.
[36] W. van Roosbroeck and W. Shockley, "Photon-radiative recombination of electrons and holes in germanium," *Phys. Rev.*, vol. 94, no. 6, pp. 1558–1560, Jun. 1954, doi: 10.1103/PhysRev.94.1558.
[37] *Menhir Photonics Femtosecond Laser Source*, Datasheet MENHIR-1550, Menhir Photon. AG, Switzerland, Jun. 2019.
[38] J. Kim and Y. Song, "Ultralow-noise mode-locked fiber lasers and frequency combs: Principles, status, and applications," *Adv. Opt. Photon.*, vol. 8, no. 3, p. 465, Aug. 2016.
[39] P. W. Juodawlkis *et al.*, "Absorption saturation nonlinearity in InGaAs/InP p-i-n photodiodes," in *Proc. 15th Annu. Meeting IEEE Lasers Electro-Optics Soc.*, vol. 2, Nov. 2002, pp. 426–427.
[40] *Microwave Analog Signal Generator*, Datasheet E8257D, Keysight, Santa Rosa, CA, USA, Feb. 2016.
[41] *Rubidium RF/Microwave Signal Generator*, Datasheet MSG36241A, Anritsu, Atsugi, Japan, Nov. 2021,
[42] T. R. Schibli *et al.*, "Optical frequency comb with submillihertz linewidth and more than 10 W average power," *Nature Photon.*, vol. 2, no. 6, pp. 355–359, May 2008.
[43] M. Kalubovilage, M. Endo, and T. R. Schibli, "Ultra-low phase noise microwave generation with a free-running monolithic femtosecond laser," *Opt. Exp.*, vol. 28, no. 17, p. 25400, Aug. 2020.

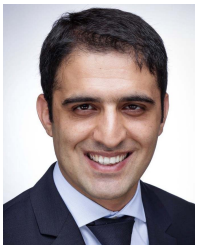

Meysam Bahmanian received the B.Sc. degree from Amirkabir University, Tehran, Iran, in 2007, and the M.Sc. degree from the University of Freiburg, Freiburg im Breisgau, Germany, in 2016. He is currently pursuing the Ph.D. degree at Paderborn University, Paderborn, Germany.

His research interests include low-noise systems, RF and mm-wave IC design, silicon photonics, and optoelectronic systems.

J. Christoph Scheytt (Member, IEEE) received the M.Sc. and Ph.D. (Hons.) degrees from Ruhr University Bochum, Bochum, Germany, in 1996 and 2000, respectively.

In 2000, he co-founded advICo microelectronics GmbH, Recklinghausen, Germany, a German IC design house for radio-frequency integrated circuit (RFIC) and fiber-optic IC design. For six years, he served as the CEO of advICo microelectronics GmbH. From 2006 to 2012, he was with Head of the Circuit Design Department, IHP Leibniz Institute for High Performance Microelectronics, Frankfurt (Oder), Germany. In 2012, he was appointed as a Full Professor of Circuit Design at Paderborn University, Paderborn, Germany, and a Research Group Leader at the Heinz Nixdorf Institute, Paderborn. Since 2016, he has been the Chairperson of the Board of Directors of the Heinz Nixdorf Institute. Since 2018, he has been the Leader of the Priority Programme "Ultrafast Electronic-Photonic Integrated Systems for Ultrafast Signal Processing" SPP 2111 of Deutsche Forschungsgemeinschaft, Bonn, Germany. He has authored or coauthored more than 180 refereed journal articles and conference contributions. He holds 20 patents. His research interests focus on high-frequency and broadband IC design for communications and sensing, IC design with silicon germanium (SiGe) bipolar CMOS (BiCMOS) and complementary metal-oxide-semiconductor (CMOS) technologies, and silicon photonics.